The Retrieval and Validation of Doppler Velocity Estimates from Range Imaging

PHILLIP B. CHILSON

Cooperative Institute for Research in Environmental Sciences, University of Colorado, and NOAA/Environmental Technology Laboratory, Boulder, Colorado

ABSTRACT

Range imaging (RIM) is used to describe a constrained optimization signal-processing method that can be applied to wind profilers capable of operating over a small set of distinct transmitter frequencies. The results of the signal-processing method are typically high-resolution maps of the backscattered power as a function of range. In this paper it is discussed how RIM processing can be implemented in order to additionally obtain high-resolution estimates of the Doppler velocity. The method has been demonstrated using data from a 915-MHz tropospheric profiler located in Platteville, Colorado. Examples of data collected during an experiment conducted on 10 April 2001 are presented. In this experiment the radar was operated alternately in two different modes. The cycle time for the two modes was about 50 s. The particular operation of the radar allowed comparison of radar reflectivity (η) and vertical velocity (V) measurements collected using the two modes. In the first mode, 2-μs pulses were transmitted and RIM processing was used to produce estimates of η and V on a grid with a separation of only 15 m. Without RIM processing the range resolution of the data would have been 300 m. In the second mode, 0.5-μs pulses were used, corresponding to a range resolution of 75 m. Estimates of η and V were then obtained from these data through conventional Doppler spectral processing. A conditional averaging method was used to process the reflectivity and vertical velocity data from the two modes. It is shown that the RIM-processed data can be used to resolve structures in the height profiles of η and V on scales less than those of the conventional range resolution of the radar as dictated by the pulse width.

1. Introduction

The term ''radar wind profiler'' is generally used to describe a class of pulsed Doppler radars that transmit radio waves vertically or near vertically and receive backscattered signals from the refractive-index fluctuations of the optically clear atmosphere. The strength and Doppler shift of the echo provide information on the structure and dynamics of the atmosphere. The range resolution of pulsed radars is defined as $c\tau/2$, where c is the speed of light and τ is the duration or width of the transmitted pulse. Clearly, the resolving power of the radar can be increased by decreasing τ. However, this approach carries with it two drawbacks. First, the transmission of shorter pulses necessitates a greater bandwidth, which is limited by hardware and frequency licensing constraints. Second, shorter pulses carry less energy, which affects the detectability of atmospheric structures. Several methods, such as the use of pulse coding (Schmidt et al. 1979) and deconvolution (Röttger and Schmidt 1979), have been proposed in order to improve range resolution while eliminating these drawbacks.

Corresponding author address: Dr. Phillip B. Chilson, NOAA–CIRES Environmental Technology Laboratory, 325 Broadway, R/ET2, Boulder, CO 80305-3328.
E-mail: phillip.chilson@noaa.gov

Recently, multiple-frequency imaging approaches have also been discussed in the literature as means of improving upon range resolution. In these methods the wind profiler alternately transmits and receives two or more radio signals that are slightly shifted in frequency with respect to one another. That is, a wind profiler could be configured to cycle through a set of N discrete frequencies within $[f_0 - \Delta f/2, f_0 + \Delta f/2]$, where f_0 is the center frequency and Δf is the width of that frequency window. Note that the maximum value of Δf is likewise limited by hardware and frequency licensing constraints. The time series of received in-phase and quadrature radar output voltages, after being down-converted to the Doppler frequency, which we will refer to as the Doppler radar signal, are recorded for each frequency f_n, where $n = 1, \ldots, N$. The manner in which the time series data are processed to improve resolution depends upon the method being implemented.

In this paper we consider a multiple-frequency signal-processing method known as range imaging (RIM) (Palmer et al. 1999) or frequency domain radar interferometric imaging (FII) (Luce et al. 2001). In the RIM technique, estimates of the cross-correlation function (or alternatively the cross spectrum) are obtained from the Doppler radar signals recorded at different frequencies. These form what is known as the visibility function. The visibilities are then used to calculate the atmo-

spheric brightness using various inversion methods. The brightness is representative of the atmospheric back-scattered power as a function of range. The terms "visibility" and "brightness" are typically expressed as functions of angle (e.g., such as used in radio astronomy and atmospheric imaging using multiple receive antennas). In this presentation we will only discuss the range dependence. Combined angular and range imaging has been discussed in Yu and Palmer (2001). The RIM brightness estimates are calculated for selected range intervals that are smaller than $c\tau/2$. Because the atmospheric brightness is directly proportional to the radar backscattered power, the technique can be used to retrieve finescale structures in the reflectivity field. In some respects RIM is simply an extension of the older frequency domain interferometry (FDI) technique described in Franke (1990).

Although a relatively new technique, RIM has already been implemented on various radar systems and demonstrated in several field experiments. Some examples of these applications made at a very high frequency (VHF) include Luce et al. (2001), Chilson et al. (2001), Palmer et al. (2001), Muschinski et al. (2001), and Smaïni et al. (2002). Recently, the technique has also been implemented at an ultrahigh frequency (UHF) (Chilson et al. 2003). Improved estimates of the atmospheric reflectivity obtained with FDI and RIM have been used to investigate the structure of Kelvin–Helmholtz instabilities, the dynamics of subsidence inversion layers, small amplitude atmospheric waves, etc.

References to range imaging that appear in the literature to date have considered only brightness as a product of RIM processing. We demonstrate how the high-resolution estimates of the first normalized moment of the Doppler spectrum (or Doppler velocity) also can be obtained through the RIM technique. First, a brief review of range imaging is presented in section 2, in which the Fourier and Capon methods are discussed. The experimental setup of the Platteville, Colorado, 915-MHz radar experiment, including how the frequency switching is accomplished, is described in section 3. In section 4 a discussion relating to data analysis, including phase calibration and data processing, is given. Experimental results are then presented in section 5. The significance of the results are addressed in section 6. Finally, the conclusions are given in section 7.

2. Theory

The fundamental principles of RIM are very similar to those for coherent radar imaging (CRI), which has been extensively discussed in such works as those of Woodman (1997), Palmer et al. (1998), Hysell (1996), Chau and Woodman (2001), and Yu and Palmer (2001). Whereas CRI uses radar signals from multiple receive antennas to image angles, in RIM different radar frequencies are used to image range. The Doppler radar signal from the N radar frequencies are represented as

$s_n(t)$, where t is time and $n = 1, \ldots, N$. We begin by creating a composite Doppler radar signal composed of the weighted sums of the original data through the equation

$$\tilde{s}_j(t) = \sum_{n=1}^{N} w_{jn} s_n(t). \qquad (1)$$

The index j is used to designate a particular "subgate" index as explained below. We will refer to $\tilde{s}_j(t)$ as the synthesized Doppler radar signal.

Now the question becomes one of estimating the values of the weighting matrix $\mathbf{w}$ (w_{jn} are components of $\mathbf{w}$). We wish to focus the sensitivity of the radar at a specific range. This is accomplished by adjusting the phase and/or amplitude of the Doppler radar signals in such a way as to produce constructive interference at the desired location in space. Typically, one creates a set of evenly spaced values in a range for which $\mathbf{w}$ should be calculated. The collective set of range values is referred to as subgates and is indexed by j in (1). That is, for each range subgate j, a weighting vector of length N is calculated and used to find $\tilde{s}_j(t)$. More information concerning subgates is given in section 4b. Note that $\mathbf{w}$ must be calculated for each time step t. There are many algorithms for calculating $\mathbf{w}$ (Palmer et al. 1999; Luce et al. 2001; Yu and Palmer 2001; Smaïni et al. 2002).

One of the inversion techniques that is often used in angular imaging or beam forming is the Fourier method. For the case when the Fourier method is applied to RIM, the weighting matrix is chosen by simply adjusting the phases of the radar signals such that constructive interference occurs at a particular range of interest. This is equivalent to what is done, for example, in poststatistic steering for the multiple-receiver analog (Röttger and Vincent 1978). The components of the weighting matrix in the Fourier method are then written as

$$w_{jn} = \exp(i2k_n r_j), \qquad (2)$$

where $k_n = 2\pi/\lambda_n$ is the wavenumber for the nth frequency and r_j is the subgate range. One of the utilities of Fourier RIM is the simplicity of its mathematical representation and implementation.

Another inversion technique is the Capon method (Capon 1969). In this application the weighting matrix is obtained through adaptive signal processing. That is, the Doppler radar signal is used in estimating $\mathbf{w}$. For Capon RIM, a constrained optimization procedure as described in Palmer et al. (1998) is used. The solution of the optimization can be found, for example, in Palmer et al. (1999) and Luce et al. (2001). The Capon method has been shown to be superior to the Fourier method in sidelobe suppression. However, because the method is adaptive, the performance depends on the atmospheric conditions being measured.

In the past, RIM processing has only been used to estimate the brightness, which is directly proportional
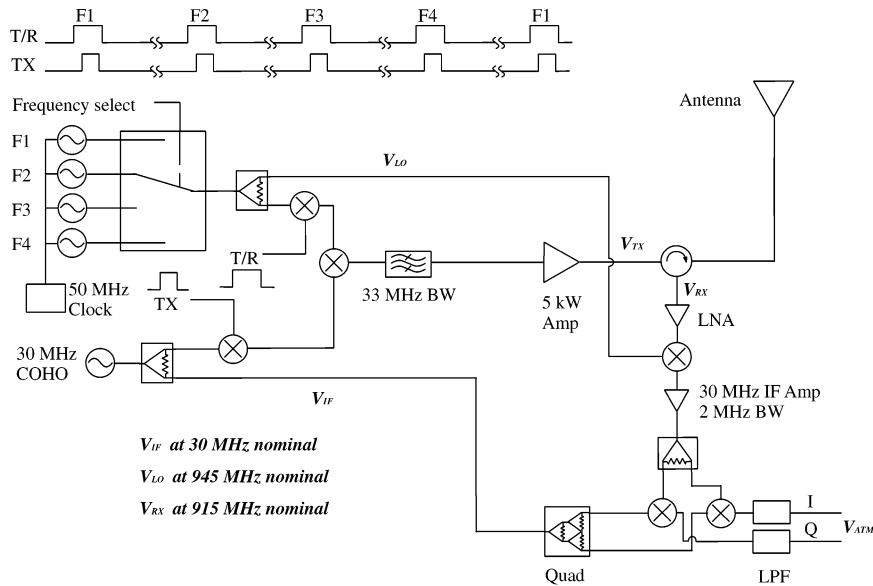
FIG. 1. Block diagram of the Platteville 915-MHz tropospheric profiler and the signal flows illustrating the application of range imaging.

to the echo power. As we see from (1), once the weighting matrix is known, then it becomes a simple task to calculate values for the synthesized Doppler radar signals for each subgate. Then, conventional Doppler signal processing as discussed in section 4 can be applied.

3. Experiment

Results are presented from an experiment that was conducted in Colorado on 10 April 2001 using the Platteville 915-MHz tropospheric profiler. The profiler was formerly located at Denver's Stapleton Airport as part of the Colorado network (Strauch et al. 1984). It is now located at the Platteville Atmospheric Observatory (40.19°N, 104.73°W, 1521 m MSL), which is jointly operated by the Environmental Technology Laboratory and the Aeronomy Laboratory, both of the National Oceanic and Atmospheric Administration (NOAA), and the Cooperative Institute for Research in Environmental Sciences (CIRES) at the University of Colorado.

The solid-state transmitter for the Platteville 915-MHz tropospheric profiler originally delivered 5.5-kW peak power, but now delivers 4.8 kW. The power amplifier and antenna have more than a 10-MHz bandwidth. The transmitted pulse is nominally generated by mixing a pulsed sample of the 945-MHz local oscillator (LO) with a pulsed sample of the 30-MHz coherent oscillator (COHO). During the experiment, the profiler was cycled through four alternating frequencies: 914, 914.33, 915.33, and 916 MHz. The frequency was switched every interpulse period, which for this experiment was 67 μs. See Chilson et al. (2003) for more details.

The block diagram in Fig. 1 shows how the four frequencies are multiplexed on a pulse-to-pulse basis. Each pulse has an independent LO frequency $f_{LO}^{(n)}$ and a common intermediate frequency (IF) f_{IF} of 30 MHz. The following equations provide the frequency and phase content of the signal voltages at each stage of the transmitter (TX) chain (see Fig. 1):

$$\angle V_{IF} = e^{i[2\pi f_{IF}t + \phi_{IF}]},$$

$$\angle V_{LO} = e^{i[2\pi f_{LO}^{(n)}t + \phi_{LO}^{(n)}]},$$

$$\angle V_{TX} = e^{i\{2\pi[f_{LO}^{(n)} - f_{IF}]t + [\phi_{LO}^{(n)} - \phi_{IF}]\}}. \quad (3)$$

The initial random phases for the oscillators are denoted by ϕ_{IF} and ϕ_{LO}. Although a phasor notation has been used, in actuality only the real part of the equations are retained. By way of example, assume that a point scatterer is located at range $\tilde{r}$. The frequency and phase of the reflected signal (RX) will then have the following form:

$$\angle V_{RX} = \exp\langle i\{2\pi(f_{LO}^{(n)} - f_{IF})t + [\phi_{LO}^{(n)} - \phi_{IF}] + 2\pi f_D^{(n)}t - 2k_n(r_0 + \tilde{r})\}\rangle, \quad (4)$$

where $f_D^{(n)}$ is the Doppler frequency and is dependent on the LO frequency. The term r_0 is the system delay, which includes delays through the transmitter and receiver chains.

A noteworthy aspect of the experiment is that the profiler was operated in two modes that were interleaved with one another. In the first mode, 2-μs (300-m resolution) pulses were transmitted and then sampled at 1 MHz (150-m spacing). In the second mode, 0.5-μs (75-m resolution) pulses were transmitted and then sampled at 2 MHz (75-m spacing). In both cases 60 time-domain averages were computed, which resulted in a Nyquist

velocity of 5.1 m s^{-1}. The profiler was operated alternately in the first mode for 31 s and in the second mode for 18.4 s. In both modes the antenna beam was oriented vertically. The height ranges for the first and second modes extended from 480 to 5730 m and from 1080 to 3105 m above ground level, respectively. A more detailed description of the experiment is given in Chilson et al. (2003).

4. Analysis

a. Phase calibration

Equation (1) will only create constructive interference at a specified subgate range r_j if it can be assumed that the radar signals $s_n(t)$ are properly calibrated. In contrast, if each radar signal has a completely independent and random initial phase, the simple weighting matrix **w** will not perform as expected. Therefore, a proper RIM experiment must include some mechanism for phase calibration. Fortunately, the design of the Platteville RIM experiment eliminates many sources of phase offset.

After coherent integration, the phase angle of the baseband signal for the Platteville UHF tropospheric profiler has the following form:

$$\angle s_n(t) = \exp\{i[2\pi f_D^{(n)}t - 2k_n(r_0 + \tilde{r})]\}. \quad (5)$$

Note that $s_n(t)$ is what we call the Doppler radar signal. It is emphasized that the initial random phase terms have been eliminated through the coherent detection process. However, the phase shift due to system delay is still present.

Given the overall bandwidth usually used with the RIM technique, a valid assumption is that the Doppler shifts from the different frequencies are approximately equivalent. Using this assumption and substituting (5) into (1), the phase angle of the signal resulting from the Fourier RIM process can be shown to have the following form:

$$\angle \tilde{s}_j(t) = \exp(i2\pi f_D t) \sum_{n=1}^{m} \exp\{-i2k_n[(r_0 + \tilde{r}) - r_j]\}. \quad (6)$$

It is obvious from (6) that the maximum power in $s_n(t)$ would result when $r_j = r_0 + \tilde{r}$, which is not the location of the assumed point scatterer. Actually, the maximum occurs at a range corresponding to the scatterer location plus the inherent system delay. Although (6) has been derived by assuming a point scatterer, the result is valid for nondiscrete scatter, such as for Bragg scatter. Likewise, similar arguments as those presented above apply when the Capon method is used to calculate the weighting vector.

The radar was calibrated by feeding V_{TX} through an ultrasonic delay line. The delay for this case was t_{delay} = 9.983 μs. This has the effect of introducing a large-amplitude signal of known phase shift into (5). After RIM processing, the signal is interpreted as having come from a range given by $r_j = r_0 + (c\, t_{delay})/2$. It then becomes a simple task to solve for r_0.

In addition to using an ultrasonic delay line, a robust calibration procedure can be obtained by incoherently averaging atmospheric data over a long time period and over numerous range gates. One would expect the power distribution to peak at the center of the range gate, given the effect of the range weighting function. Therefore, r_0 could be calculated as the range shift away from the center of the gate after significant averaging. The estimate of r_0 calculated using this method was very similar to that found using an ultrasonic delay line.

b. Data processing

All Doppler radar signals collected during the experiment were processed using conventional spectral processing. Throughout the text, we refer to the method of using moment calculations from a single-frequency Doppler autospectrum to derive estimates of the backscattered power, radial velocity, and the variance of the radial velocity as conventional spectral processing (e.g., Woodman 1985). Because multiple-frequency data were collected, spectra were calculated for each of the operating frequencies separately and then averaged in both time and frequency. We will refer to the values of signal-to-noise ratio (SNR) and Doppler velocity calculated from the original Doppler radar signals' 300-m-resolution data as SNR_{STD300} and V_{STD300}, respectively. Correspondingly, these quantities calculated from the 75-m-resolution data will be written as SNR_{STD75} and V_{STD75}.

Overview plots showing values of SNR and Doppler velocity calculated using conventional spectral processing for 300- and 75-m-resolution data are given in Figs. 2 and 3, respectively. Note that the SNR data are plotted over a different range in Fig. 3 than used for Fig. 2. One expects a reduction in SNR_{STD75} of 6 dB compared to SNR_{STD300} on account of the smaller pulse width. The region of the greatest SNR is located just below an altitude of 1500 m. From both the SNR data shown in Fig. 3 and the analysis of this dataset presented in Chilson et al. (2003), we know that a narrow scattering layer corresponding to large backscattered power is located within this region. However, it is difficult to detect much vertical structure in the SNR data presented in Fig. 2. The plots of Doppler velocity data show overall fluctuations in the vertical velocity field with an apparent period lasting between 30 and 45 min. In the region of the greatest SNR, lower period oscillations can be observed in the vertical velocity.

RIM processing using the Fourier and Capon methods was performed on the 2-μs data shown in Fig. 2. The sample spacing was set at 15 m. That is, each 300-m range gate was partitioned into 20 subgates. A value of 15 m was chosen as a compromise between computation time and resolution. For the RIM processing, one weighting vector was calculated for each subgate and
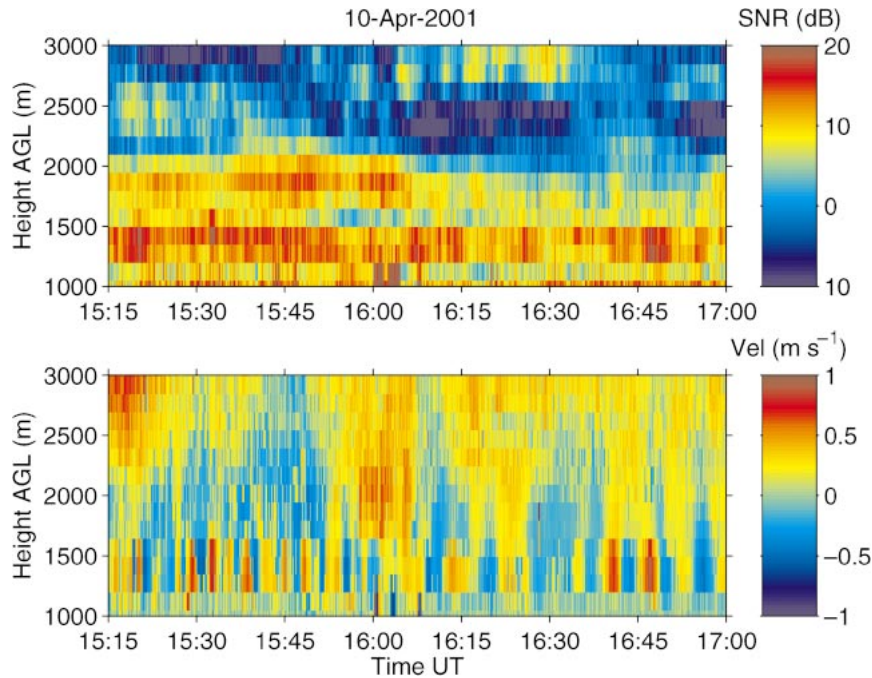
FIG. 2. Range–time pseudocolor plots of SNR (SNR_{STD300}) and Doppler velocity (V_{STD300}) computed from 300-m-resolution pulses sampled every 150 m.

for each sampling time of 31 s. Because the extent of the 300-m range gates overlapped with one another (i.e., they were oversampled), two independent estimates of the weighting vector were obtained for most of the subgates. This is illustrated in Fig. 4. In these cases, the weighting vector corresponding to the highest value of SNR was used to calculate synthesized radar signals using (1). Conventional spectral processing was then applied. We will refer to the values of SNR and Doppler velocity calculated in this manner as SNR_{RIM} and V_{RIM}, respectively.

An example of Capon RIM processing for a small time–height sampling window taken from the data shown in Fig. 2 is presented in Fig. 5. The data were collected over 2-min intervals centered at 0730 local time (LT). The three left panels show Doppler spectra obtained for three consecutive range gates observed using a 2-μs pulse and without RIM processing. We have chosen a velocity window smaller than the Nyquist velocity to show greater detail in the signal portion of the spectra. Recall that the sampling volumes overlap by 150 m. Also shown are the normalized first moments of the spectra (V_{STD800}) as dashed lines. The right panel shows a Doppler spectrograph of the 15-m subgated RIM results. These results were generated from the same Doppler radar signals that were used to calculate the spectra shown to the left. Only the signal processing has changed. The solid line traces the normalized first moments of the spectra computed from the synthesized Doppler radar signals (V_{RIM}). The solid circles indicate

the normalized first moments of the three Doppler spectra shown on the left.

For the present study we have chosen to only show RIM results obtained using the Capon method. As has already been mentioned, for the RIM application the Fourier technique is somewhat inferior to the Capon method. For example, the Capon inversion algorithm provides better sidelobe suppression than does the Fourier method. A comparison of some Fourier and Capon RIM results from this dataset is given in Chilson et al. (2003). Although not shown here, the synthesized Doppler radar signals obtained using the Fourier method are certainly similar to those obtained for Capon processing. The Fourier RIM results, however, exhibit more range sidelobe contamination and a somewhat reduced resolution.

It is difficult to determine whether the vertical structure in the Doppler (vertical) velocity is real or an artifact of the processing. Figure 6 shows profiles of the Doppler velocity estimates obtained using the 2-μs pulse (V_{STD800}), 0.5-μs pulse (V_{STD75}), and RIM processing (V_{RIM}). The RIM data follow the structure of the V_{STD75} data reasonably well. Note that the V_{STD800} data, although sampled every 150 m, are not able to capture the vertical structure in the vertical velocity field. Furthermore, notice that the V_{STD800} values are biased toward zero. This is a result of the reversal in the vertical velocity values from positive to negative within an altitude range of 1300 and 1400 m. Recall that the underlying resolution of the 2-μs pulse is 210 m. The bias is primarily attributed to the effect of volume averaging.
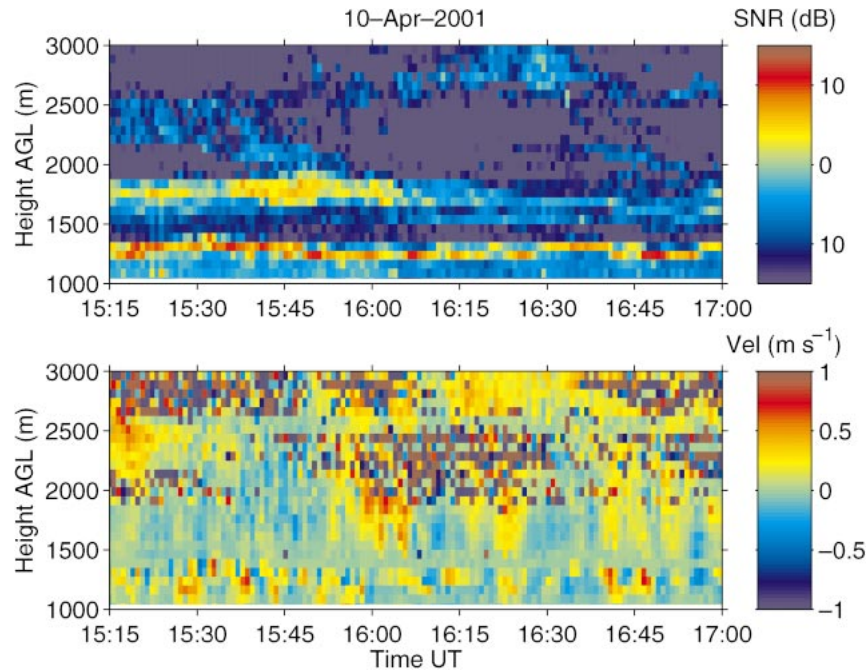
FIG. 3. Range–time pseudocolor plots of SNR (SNR$_{STD75}$) and Doppler velocity (V_{STD75}) computed from 75-m-resolution pulses.

The results of the RIM processing for the complete dataset are shown in Fig. 7. The data shown were calculated from the synthesized Doppler radar signals. In the plot of SNR data, we see similar structures to those that were presented in Chilson et al. (2003) as backscattered power. Furthermore, it is easy to see that both Figs. 7 and 3 contain similar features in both SNR and velocity. There is a persistent narrow scattering layer at an altitude of about 1300 m, and there are billow struc-
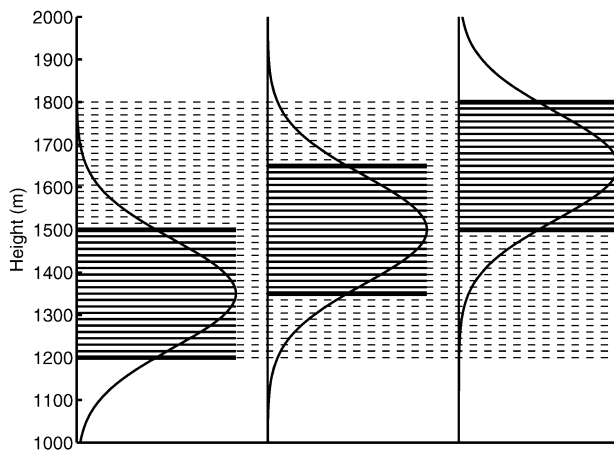

FIG. 4. Illustration of the sampling scheme and subgating used during the RIM experiment and data processing. The three Gaussian-shaped curves represent three consecutive (in height) range weighting functions for a 2-μs pulse width. The heavy solid horizontal lines delineate the standard width of a range gate as given by $c\tau/2$. The dashed horizontal lines show the boundaries of the subgates for a 15-m subgate spacing.

tures located just below an altitude of 2000 m. The new aspect of the present analysis is the ability to estimate Doppler velocities for individual subgates. Although the same temporal patterns in the vertical velocity data appear in the lower panel, we find more vertical structure in the RIM-processed velocities. To fully ascertain how effective the RIM processing has been, a more statistical comparison is necessary.

5. Comparison of conventional and RIM processing

In this section we compare the reflectivities and Doppler velocities calculated using conventional spectral processing on the original and RIM-processed Doppler radar signals. Reflectivities are estimated by finding the range-corrected values of backscattered power. We use echo power divided by the appropriate value of r^2, where r is range. Using the same naming convention as introduced earlier, we define η_{STD800}, η_{STD75}, and η_{RIM} for the reflectivity values corresponding to the 300-m-resolution data, 75-m-resolution data, and the RIM data, respectively.

We have used conditional averaging in our comparison of the reflectivities (η_{STD75} and η_{RIM}) and Doppler velocities (V_{STD75} and V_{RIM}). For example, the conditional average of η_{RIM} for a specified values of η_{STD75} was computed as follows. The values of η_{STD75} were first partioned into 30 logarithmically spaced bins in the range from 10^7 to 10^{11}. Note that these values include an unknown scaling factor. Because the resolutions of
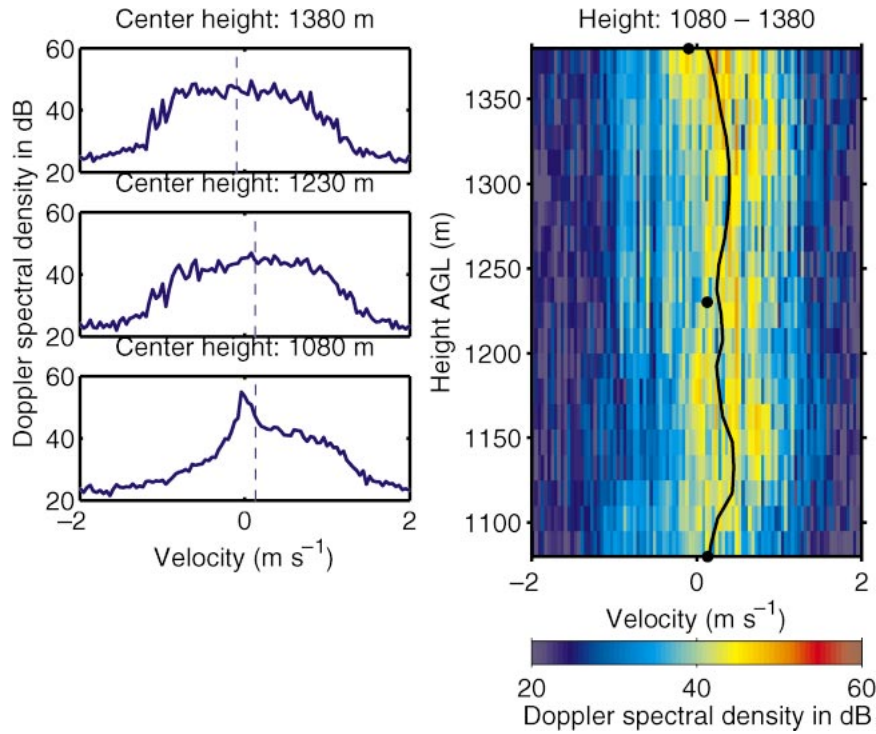
FIG. 5. (left) Results of coventional spectral processing on Doppler radar signals from 300-m-resolution pulses sampled every 150 m. The vertical dashed lines show the normalized first moments of the spectra (V_{STD300}). (right) The spectrograph for synthesized Doppler radar signals computed with a 15-m subgate spacing using the Capon method. The solid line shows the normalized first moments of the spectra (V_{RIM}). The solid circles represent the normalized first moments shown to the left.

η_{STD75} and η_{RIM} do not match, we have chosen to use η_{RIM} calculated for those subgates that are most closely centered with the 75-m-resolution range gates. Each of these that corresponded to a value of η_{STD75} falling within one of the logarithmically spaced bins was further
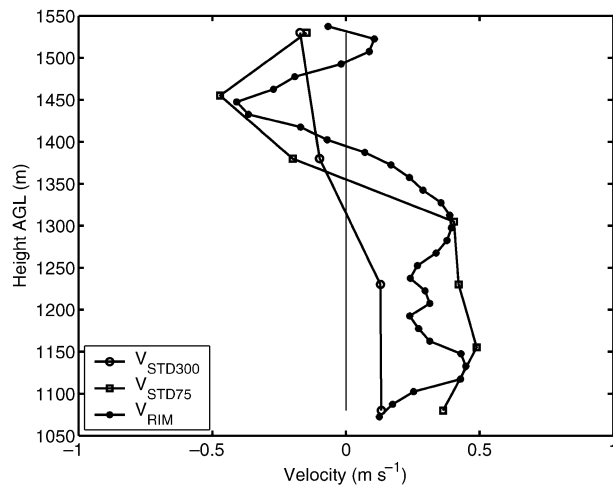

FIG. 6. Height profiles of the Doppler velocities calculated from the 300-m-resolution (V_{STD300}) data, 75-m-resolution (V_{STD75}) data, and RIM (V_{RIM}) data.

averaged together. The procedure produced a single averaged value of the RIM reflectivity for each of the bins. These are collectively written as $\langle \eta_{RIM} | \eta_{STD75} \rangle$.

Conditional averaging for $\langle V_{RIM} | V_{STD75} \rangle$ was similarly performed with the range of V_{STD75} being linearly partitioned from -1 to 1 m s^{-1}. As before, values of V_{RIM} were selected for those subgates corresponding to the center of the 75-m-resolution range gates. These were used for the comparison with η_{STD75} and the conditional average was computed as described above for each bin.

Before performing the conditional averages, the reflectivity and velocity data were divided into two separate datasets as determined by height. Based on radiosonde data from the Denver Stapleton Airport (39.77°N, 104.88°W, WMO station 72469) the air was saturated below a height of about of 1500 m AGL. Furthermore, the wind speed was light (less than 5 m s^{-1}) and the wind direction was variable below 1500 m. Above the level the wind speed began increasing with height and was coming out of the north-northeast. Therefore, we have chosen to group the reflectivity and velocity data according to height. The lower and upper regions span heights from 1000 to 1500 m and 1500 to 3000 m, respectively.

The result of the conditional average $\langle \eta_{RIM} | \eta_{STD75} \rangle$ for the lower and upper height regions are shown in the
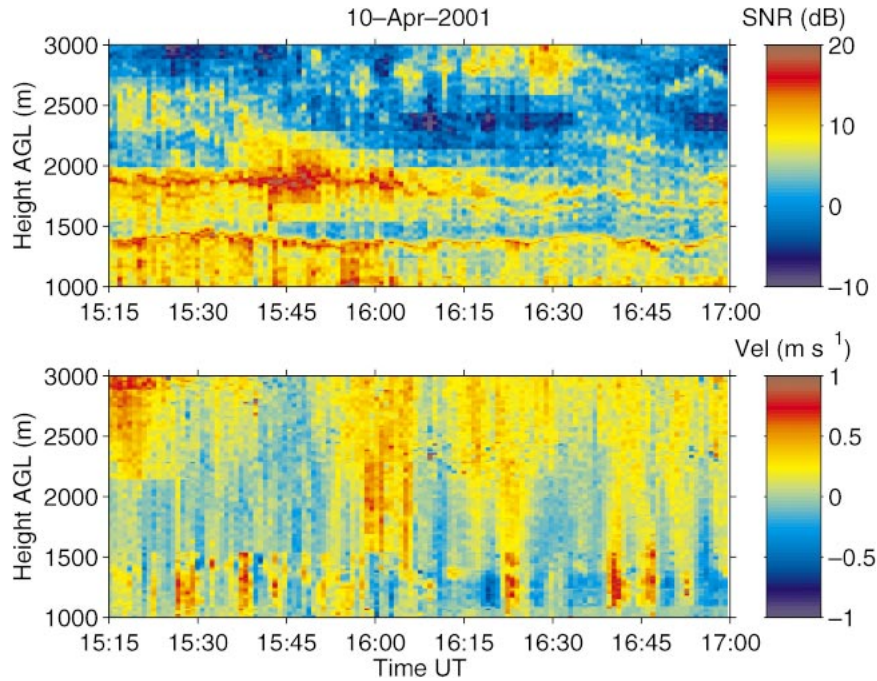
FIG. 7. Same data as shown in Fig. 2 after RIM processing.

lower right panels of Figs. 8 and 9, respectively. The reflectivity from the synthesized Doppler radar signals was subgated at a 15-m resolution. Also shown in Figs. 8 and 9 are the probability distribution functions (PDFs) of η_{STD75} and η_{RIM} and the scatterplot of η_{RIM} versus η_{STD75}. One expects a lognormal distribution for PDFs of reflectivity. This is true for the case for η_{RIM}; however, the PDF for η_{STD75} is seen to be influenced by noise and other factors.

There are a few notable features in the plots of $\langle\eta_{RIM}\,|\,\eta_{STD75}\rangle$ shown as a function of η_{STD75}. First, the values of $\langle\eta_{RIM}\,|\,\eta_{STD75}\rangle$ closely follow a linear relationship with respect to η_{STD75}. Second, the slopes of the relationships are less than 1, which may lead one to believe that the RIM processing has introduced a bias to the estimates of η_{RIM}. The reduction in slope is particularly noticeable in Fig. 8. We discuss this in more detail in the next section. Third, there is a tendency for the curves describing $\langle\eta_{RIM}\,|\,\eta_{STD75}\rangle$ to flatten out for the lower values of η_{STD75}, that is, for values of η_{STD75} small-
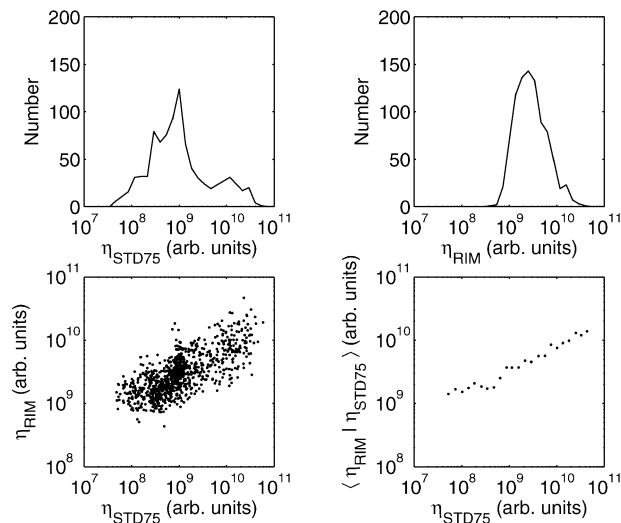

FIG. 8. Results of the conditional averaging $\langle\eta_{RIM}\,|\,\eta_{STD75}\rangle$ in the height range from 1000 to 1500 m AGL. The upper panels show the probability distribution functions for η_{STD75} and η_{RIM}. The lower left and right panels show the scatterplot and $\langle\eta_{RIM}\,|\,\eta_{STD75}\rangle$, respectively.
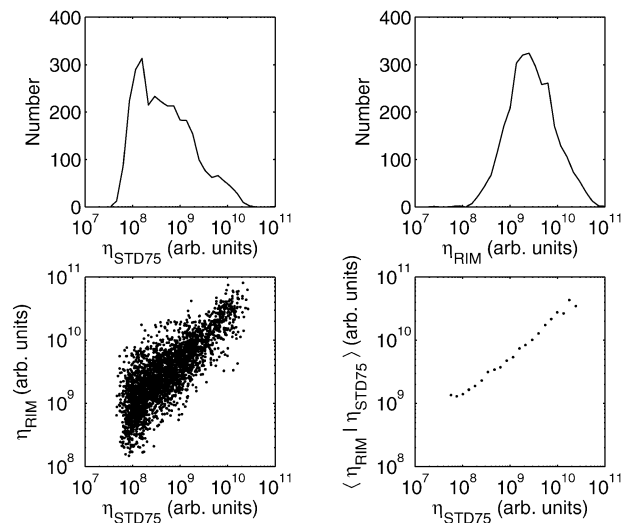

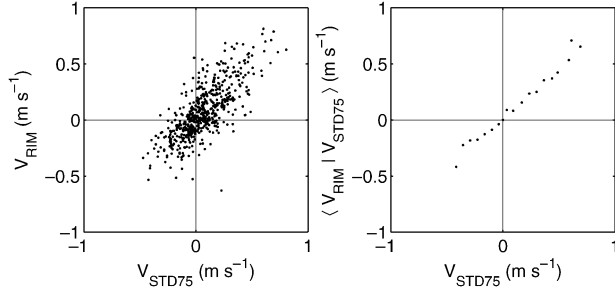FIG. 9. Same as for Fig. 8, except in the height range of 1500–3000 m AGL.

FIG. 10. Results of the conditional averaging $\langle V_{\mathrm{RIM}} | V_{\mathrm{STD75}} \rangle$ in the height range from 1000 to 1500 m AGL. The left and right panels show the scatterplot and $\langle V_{\mathrm{RIM}}/V_{\mathrm{STD75}} \rangle$, respectively.

FIG. 11. Same as in Fig. 10 in the height range from 1000 to 1500 m AGL.

er than 10^8. Here again, we defer a discussion of the significance of this result until the next section.

We now present the results of conditional averaging on the velocity data. In Figs. 10 and 11 we show the scatterplots for V_{RIM} versus V_{STD75} and the relationship between $\langle V_{\mathrm{RIM}} | V_{\mathrm{STD75}} \rangle$ and V_{STD75} for the lower and upper height regions, respectively. Only velocity data calculated from spectra with a power level greater than that of a specified threshold value were used. As for the values of $\langle \eta_{\mathrm{RIM}} | \eta_{\mathrm{STD75}} \rangle$ shown in Figs. 8 and 9, the plots of $\langle V_{\mathrm{RIM}} | V_{\mathrm{STD75}} \rangle$ versus V_{STD75} follow a linear relationship with a slope slightly less than 1 with little variation for values of V_{STD75} between about -0.2 to 0.6 m s^{-1}. The values of V_{RIM} shown in the plots of $\langle V_{\mathrm{RIM}} | V_{\mathrm{STD75}} \rangle$ tend to flatten out for V_{STD75} less than -0.2 m s^{-1} and greater than 0.6 m s^{-1}. It is encouraging to observe that the plots of $\langle V_{\mathrm{RIM}} | V_{\mathrm{STD75}} \rangle$ versus V_{STD75} passes through the origin for both height regions, which indicates that no offsets have been introduced through the RIM processing.

6. Discussion

We now examine the results presented in the last section within a more formal framework. To begin, consider two random variables x and y. Assume that x and y are samples, taken by two independent volume-averaging sensors, of the same random spatial field $q(\mathbf{x})$, such that

$$x = \iiint G_1(\mathbf{x}')q(\mathbf{x}') \, d^3x' \quad \text{and} \qquad (7)$$

$$y = \iiint G_2(\mathbf{x}'')q(\mathbf{x}'') \, d^3x''. \qquad (8)$$

Here we have neglected noise contributions. The spatial weighting functions $G_1(\mathbf{x}')$ and $G_2(\mathbf{x}'')$ describe the sampling volumes of the two sensors. Obviously, $x = y$ if $G_1(\mathbf{x})$ and $G_2(\mathbf{x})$ are identical. That is, x and y are still random variables, but they track each other perfectly.

If $G_1(\mathbf{x})$ and $G_2(\mathbf{x})$ are different, then x and y cannot track each other perfectly but, in general, they are still correlated. The degree by which x and y do track each other can be quantified by their correlation coefficient,

$$\rho = \frac{\langle (x - \langle x \rangle)(y - \langle y \rangle) \rangle}{\sigma_x \sigma_y}, \qquad (9)$$

where $\langle \bullet \rangle$ designates an ensemble average, and σ_x and σ_y are the variances of the variables x and y, respectively.

Now let us assume that the joint PDF $p_{xy}(x, y)$ of x and y is jointly Gaussian, or jointly normal such that

$$p_{xy}(x, y) = \frac{1}{2\pi\sigma_x\sigma_y\sqrt{1 - \rho^2}} \exp\left\{ -\frac{1}{2(1 - \rho^2)} \left[\frac{(x - \langle x \rangle)^2}{\sigma_x^2} - 2\rho\frac{(x - \langle x \rangle)(y - \langle y \rangle)}{\sigma_x\sigma_y} + \frac{(y - \langle y \rangle)^2}{\sigma_y^2} \right] \right\} \qquad (10)$$

(e.g., Newland 1993, p. 18). The conditional average of y for a specified value of x is by definition

$$\langle y | x \rangle \equiv \frac{\displaystyle\int p_{xy}(x, y)y \, dy}{\displaystyle\int p_{xy}(x, y) \, dy}. \qquad (11)$$

After lengthy but elementary manipulations, we obtain for the jointly normal PDF the expression

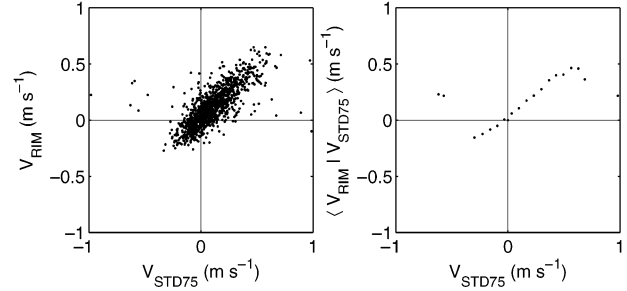$$\langle y | x \rangle = \rho\frac{\sigma_y}{\sigma_x}x. \qquad (12)$$

Therefore, the slope $s \equiv \partial \langle y | x \rangle / \partial x$ proves to be simply

$$s = \rho\frac{\sigma_y}{\sigma_x}. \qquad (13)$$

As was seen in the last section, the slopes of $\langle \eta_{\mathrm{RIM}} | \eta_{\mathrm{STD75}} \rangle$ versus η_{STD75} are consistently less than 1, which indicates that either $\rho < 1$ or $\sigma_{\eta_{\mathrm{RIM}}} < \sigma_{\eta_{\mathrm{STD75}}}$ or

both. The plots of the PDFs in Figs. 8 and 9 show that $\sigma_{\eta_{\text{RIM}}}$ is indeed larger than $\sigma_{\eta_{\text{STD75}}}$; however, we must also recall that the PDFs are influenced by noise contributions. In fact, the tendency of the slope to approach zero for low values of reflectivity can be attributed to noise contamination. If the reflectivities are strongly influenced by noise, then ρ should tend toward zero. Clearly, the conditional average $\langle y | x \rangle$, where x and y are completely uncorrelated random signals would simply be constant for all values of x.

When examining the plots of η_{RIM} versus η_{STD75} and $\langle \eta_{\text{RIM}} | \eta_{\text{STD75}} \rangle$ versus η_{STD75} one must consider how these results may be affected when the atmospheric reflectivity is highly structured along the vertical extent as was observed by Richter (1969), Eaton et al. (1995), and Muschinski and Wode (1998). Further, consider that the atmospheric radar measurements shown here were made using disparate sampling volumes on account of the different range resolutions. In such a case a localized reflecting atmospheric layer or sheet with high reflectivity could be detected in the larger sampling volume but not in the smaller. It is obvious that a decorrelation of the reflectivity estimates obtained from two dissimilar sampling volumes in this case, for example, the quantities η_{RIM} and η_{STD75}, is expected. This naturally leads to a reduction in ρ. It is not clear from these data whether the greater reduction in slope of $\langle \eta_{\text{RIM}} | \eta_{\text{STD75}} \rangle$ versus η_{STD75} for the lower height region as compared to the upper height region can be attributed to this effect.

Discussions that involve the importance of contributions from radar returns from atmospheric layers as compared with standard Bragg backscatter can be found in such works as those of Metcalf and Atlas (1973), Gage and Green (1978), and Röttger and Vincent (1978). In order for radar returns from atmospheric layers to be comparable with Bragg backscatter, the layer thickness must be less than about half a wavelength (Gossard et al. 1984). Balsley et al. (2003) have reported a temperature step of 1 K over a height range of only 5 cm at a height of about 180 m AGL. Under these conditions the radar return is referred to as "partial reflection." We should bear in mind that reflectivity is defined for volume filling scatter. As stated in Gossard et al. (1984): "Under conditions when partial reflection can be important, the return is from only a tiny fraction of the resolution cell of the radar. Therefore, the return is proportional to the number of layers, and the physical basis for layer number and spacing becomes very important." In such a case, it is not correct to use the term "reflectivity." For the sake of the present analysis, though, we will associate the radar return from the layers as being an equivalent reflectivity.

Next we reconsider the results shown in Figs. 10 and 11. As for the reflectivities, the slope of the conditionally averaged velocity data plotted against the values of V_{STD75} is consistently less than 1 and approaches zero for extreme values of velocity. Whenever the vertical velocity data contain distinct discontinuities in height, the reduc-

tion in slope can again be understood in terms of sampling volumes that have dissimilar range resolutions. An example height-dependent structure in the vertical velocity field has already been shown in Fig. 6.

What mechanisms are capable of generating such discontinuities in the vertical velocity field with height? One possible mechanism is associated with Kelvin–Helmholtz instabilities (KHIs). The vertical velocities in the vicinity of KHI have been shown to undergo abrupt changes in magnitude over an altitude range on the order of 100 m (VanZandt et al. 1979; Klostermeyer and Rüster 1980, 1981; Rüster and Klostermeyer 1983; Chilson et al. 1997). Figures 3 and 9 of Chilson et al. (2003), which deals with the same data as presently being discussed, clearly show evidence of KHI during the period of observation. This would be consistent with a decorrelation of V_{RIM} and V_{STD75}, and consequently, with a reduction in the value of the slope.

7. Conclusions

The ability to provide high-resolution profiles of radar reflectivity and Doppler velocity in the atmospheric boundary layer obviously has many advantages. The observation and monitoring of the height and thickness of the entrainment zone, internal gravity waves in stably stratified flows, and Kelvin–Helmholtz instabilities are but a few examples.

In this paper we have outlined how Doppler velocity data can be retrieved through RIM signal processing. The advantage of RIM processing over conventional spectral processing is that the velocity estimates can be obtained for each subgate. Although not discussed in this paper, it is easy to see how the method can be extended to retrieve the second central moment of the Doppler spectrum (spectral width). The technique was demonstrated using data from a UHF radar wind profiler; however, the technique can be implemented on any wind profiler capable of operating over a small set of distinct transmitter frequencies.

It was found that the slope of the conditionally averaged data $\langle \eta_{\text{RIM}} | \eta_{\text{STD75}} \rangle$ when plotted versus η_{STD75} is consistently less than 1. The same is true for the slope of $\langle V_{\text{RIM}} | V_{\text{STD75}} \rangle$ versus V_{STD75}. One may initially expect to find a slope of 1 for the conditionally averaged data collected under ideal conditions. However, a slope of 1 would actually indicate that nothing has been gained from the RIM processing. For example, for the case presented here, a slope of 1 would indicate that the same information obtained from RIM processing is available from the conventionally processed 0.5-μs pulses. That is, the higher-resolution data are not needed. This could well be true if the quantity being measured varies slowly and smoothly with height. Therefore, having a slope consistently less than 1 is a positive indicator that the RIM processing is providing the needed resolution to detect distinct range-dependent structures in the reflectivity and velocity fields.

The RIM technique has now been implemented on numerous wind profilers and mesosphere–stratosphere–troposphere (MST) radars around the world at frequencies ranging from VHF to UHF. Additionally, the technique has recently been successfully adapted to more conventional commercially available profilers such as the LAP-3000 from Vaisala, Inc. The technique is also not limited to measurements made with a vertically pointing antenna beam. For example, although not shown here, RIM has been used in conjunction with Doppler beam steering (DBS) observations to generate high spatial resolution height profiles of the horizontal wind field. These data are being used for a RIM wind validation study.

Finally, the dataset used in this study is arguably not the best suited for validating the velocity estimates obtained from RIM. It does, however, offer the advantage a direct comparison of wind estimates obtained from the same instrument, which was the underlying reason for using this dataset for the study. Additional experiments are ongoing in order to further validate the RIM technique. These experiments include horizontal wind measurements obtained from RIM-processed and conventional radar data. Complementary to these data are independent methods of estimating the winds such as rawinsondes and anemometers. Alternative methods of obtaining wind profiles including sodars and Doppler lidars should also be considered.

REFERENCES

Balsley, B. B., R. G. Frehlich, M. L. Jensen, Y. Meillier, and A. Muschinski, 2003: Extreme gradients in the nocturnal boundary layer: Structure, evolution, and potential causes. *J. Atmos. Sci.,* **60,** 2496–2508.

Capon, J., 1969: High-resolution frequency-wavenumber spectrum analysis. *Proc. IEEE,* **57,** 1408–1419.

Chau, J. L., and R. F. Woodman, 2001: Three-dimensional coherent radar imaging at Jicamarca: Comparison of different inversion techniques. *J. Atmos. Sol. Terr. Phys.,* **63,** 253–261.

Chilson, P. B., A. Muschinski, and G. Schmidt, 1997: First observations of Kelvin–Helmholtz billows in an upper level jet using VHF frequency domain interferometry. *Radio Sci.,* **32,** 1149–1160.

——, R. D. Palmer, A. Muschinski, D. A. Hooper, G. Schmidt, and H. Steinhagen, 2001: SOMARE-99: A demonstrational field campaign for ultra-high resolution VHF atmospheric profiling using frequency diversity. *Radio Sci.,* **36,** 695–707.

——, T.-Y. Yu, R. G. Strauch, A. Muschinski, and R. D. Palmer, 2003: Implementation and validation of range imaging on a UHF radar wind profiler. *J. Atmos. Oceanic Technol.,* **20,** 987–996.

Eaton, F. D., S. A. McLaughlin, and J. R. Hines, 1995: A new frequency-modulated continuous wave radar for studying planetary boundary layer morphology. *Radio Sci.,* **30,** 75–88.

Franke, S. J., 1990: Pulse compression and frequency domain interferometry with a frequency-hopped MST radar. *Radio Sci.,* **25,** 565–574.

Gage, K. S., and J. L. Green, 1978: Evidence for specular reflection from monostatic VHF radar observations of the stratosphere. *Radio Sci.,* **13,** 991–1001.

Gossard, E. E., W. D. Neff, R. J. Zamora, and J. Gaynor, 1984: The fine structure of elevated refractive layers: Implications for over-the-horizon propogation and radar sounding systems. *Radio Sci.,* **19,** 1523–1533.

Hysell, D. L., 1996: Radar imaging of equatorial F region irregularities with maximum entropy interferometry. *Radio Sci.,* **31,** 1567–1578.

Klostermeyer, J., and R. Rüster, 1980: Radar observations and model computation of a jet stream-generated Kelvin–Helmholtz instability. *J. Geophys. Res.,* **85,** 2841–2846.

——, and ——, 1981: Further study of a jet stream-generated Kelvin–Helmholtz instability. *J. Geophys. Res.,* **86,** 6631–6637.

Luce, H., M. Yamamoto, S. Fukao, D. Helal, and M. Crochet, 2001: A frequency domain radar interferometric imaging (FII) technique based on high resolution methods. *J. Atmos. Sol. Terr. Phys.,* **63,** 201–214.

Metcalf, J., and D. Atlas, 1973: Microscale ordered motions and atmospheric structure associated with thin echo layers in stably stratified zones. *Bound.-Layer Meteor.,* **4,** 7–35.

Muschinski, A., and C. Wode, 1998: First in situ evidence for coexisting submeter temperature and humidity sheets in the lower free troposphere. *J. Atmos. Sci.,* **55,** 2893–2906.

——, P. B. Chilson, R. D. Palmer, G. Schmidt, and H. Steinhagen, 2001: Boundary-layer convection and diurnal variation of vertical-velocity characteristics in the free troposphere. *Quart. J. Roy. Meteor. Soc.,* **127,** 423–444.

Newland, D. E., 1993: *An Introduction to Random Vibrations, Spectral and Wavelet Analysis.* 3d ed. Pearson Higher Education, 480 pp.

Palmer, R. D., S. Gopalam, T.-Y. Yu, and S. Fukao, 1998: Coherent radar imaging using Capon's method. *Radio Sci.,* **33,** 1585–1589.

——, T.-Y. Yu, and P. B. Chilson, 1999: Range imaging using frequency diversity. *Radio Sci.,* **34,** 1485–1496.

——, P. B. Chilson, A. Muschinski, G. Schmidt, T.-Y. Yu, and H. Steinhagen, 2001: SOMARE-99: Observations of tropospheric scattering layers using multiple-frequency range imaging. *Radio Sci.,* **36,** 681–693.

Richter, J. H., 1969: High resolution tropospheric radar soundings. *Radio Sci.,* **4,** 1261–1268.

Röttger, J., and R. A. Vincent, 1978: VHF radar studies of tropospheric velocities and irregularities using spaced antenna techniques. *Geophys. Res. Lett.,* **5,** 917–920.

——, and G. Schmidt, 1979: High-resolution VHF radar sounding of the troposphere and stratosphere. *IEEE Trans. Geosci. Electron.,* **17,** 182–189.

Rüster, R., and J. Klostermeyer, 1983: VHF radar observations of a Kelvin–Helmholtz instability in a subtropical jet stream. *Geophys. Astrophys. Fluid Dyn.,* **26,** 107–116.

Schmidt, G., R. Rüster, and P. Czechowsky, 1979: Complementary code and digital filtering for detection of weak VHF radar signals from the mesosphere. *IEEE Trans. Geosci. Electron.,* **GE-17,** 154–161.

Smaïni, L., H. Luce, M. Crochet, and S. Fukao, 2002: An improved high-resolution processing method for a frequency domain interferometric FII technique. *J. Atmos. Oceanic Technol.,* **19,** 954–966.

Strauch, R. G., D. A. Merritt, K. P. Moran, K. B. Earnshaw, and D. V. de Kamp, 1984: The Colorado wind-profiling network. *J. Atmos. Oceanic Technol.,* **1,** 37–49.

VanZandt, T. E., J. L. Green, and W. L. Clark, 1979: Buoyancy waves in the troposphere: Doppler radar observations and a theoretical model. *Geophys. Res. Lett.,* **6,** 429–432.

Woodman, R. F., 1985: Spectral moment estimation in MST radars. *Radio Sci.,* **20,** 1185–1195.

——, 1997: Coherent radar imaging: Signal processing and statistical properties. *Radio Sci.,* **32,** 2372–2391.

Yu, T.-Y., and R. D. Palmer, 2001: Atmospheric radar imaging using spatial and frequency diversity. *Radio Sci.,* **36,** 1493–1504.